

Accretion-Induced Collapse of Dark Matter Admixed White Dwarfs - II: Rotation and Gravitational-wave Signals

SHUAI ZHA,¹ MING-CHUNG CHU,¹ SHING-CHI LEUNG,² AND LAP-MING LIN¹

¹*Department of Physics and Institute of Theoretical Physics, The Chinese University of Hong Kong, Shatin, N.T., Hong Kong S.A.R., China*

²*Kavli Institute for the Physics and Mathematics of the Universe (WPI), The University of Tokyo Institutes for Advanced Study, The University of Tokyo, Kashiwa, Chiba 277-8583, Japan*

(Received xxx, xxxx; Revised xxx, xxxx; Accepted xxx, xxxx)

Submitted to ApJ

ABSTRACT

We present axisymmetric hydrodynamical simulations of accretion-induced collapse (AIC) of dark matter (DM) admixed rotating white dwarfs (WD) and their burst gravitational-wave (GW) signals. For initial WD models with the same central baryon density, the admixed DM is found to delay the plunge and bounce phases of AIC, and decrease the central density and mass of the proto-neutron star (PNS) produced. The bounce time, central density and PNS mass generally depend on two parameters, the admixed DM mass M_{DM} and the ratio between the rotational kinetic and gravitational energies of the inner core at bounce $\beta_{\text{ic,b}}$. The emitted GWs have generic waveform shapes and the variation of their amplitudes h_+ show a degeneracy on $\beta_{\text{ic,b}}$ and M_{DM} . We found that the ratios between the GW amplitude peaks around bounce allow breaking the degeneracy and extraction of both $\beta_{\text{ic,b}}$ and M_{DM} . Even within the uncertainties of nuclear matter equation of state, a DM core can be inferred if its mass is greater than $0.03 M_{\odot}$. We also discuss possible DM effects on the GW signals emitted by PNS g-mode oscillations. GW may boost the possibility for the detection of AIC, as well as open a new window in the indirect detection of DM.

Keywords: dark matter – gravitational waves – white dwarfs – stars: supernovae

1. INTRODUCTION

It is commonly known that dark matter (DM) constitutes approximately 84% of the matter in the universe (Planck Collaboration et al. 2018). The existence of DM is crucial for explaining the flattening of galactic rotation curve (Einasto et al. 1974) and the Bullet cluster observation (Lee & Komatsu 2010), but the nature of DM is largely unknown despite decades of searches (e.g., Ren et al. 2018) and the many hypothetical candidates (Bertone & Hooper 2018). DM is believed to play an important role in the formation of cosmic microwave background anisotropies (CMB) and large-scale structures. An interesting question is what impacts they might have on small-scale structures, such as stars and supernovae. DM admixed in star provide extra gravity

to alter the stellar structure (Brito et al. 2015) and additional heating/cooling to alter its surface luminosity and lifespan (Bramante 2015; Choplin et al. 2017).

With a very high central density (ρ_c), compact stars such as white dwarfs (WD, $\rho_c \sim 10^9\text{--}10^{10} \text{ g/cm}^3$) and neutron stars (NS, $\rho_c \sim 10^{14\text{--}15} \text{ g/cm}^3$) provide great observational playgrounds for detecting DM (Leung et al. 2011, 2013; Graham et al. 2018; Ellis et al. 2018), complementary to direct detection experiments. Fuller & Ott (2015) proposed that DM-induced collapse of NSs can explain the missing pulsar problem at the galactic center and the fast radio burst phenomena. Also, there have been studies on the effects of DM on the thermonuclear explosions of WDs, i.e., Type Ia supernovae (SNe Ia). Bramante (2015) studied the accretion of PeV-scale DM by WDs and found that this can explain the age-luminosity anti-correlation relation for SNe Ia. Graham et al. (2015) suggested that the transit of primordial black holes (PBH) can ignite SNe Ia through heating by dynamical friction and the scenario

can put some constraints on the PBH mass. [Leung et al. \(2015a\)](#) found that DM admixture decreases the canonical WD Chandrasekhar mass ($M_{\text{Ch}} \sim 1.44 M_{\odot}$), and their subsequent hydrodynamical simulations showed that DM admixed SNe Ia synthesize less ^{56}Ni and can fit some sub-luminous SN Ia light curves.

While SNe Ia have been studied extensively (see the review in [Hillebrandt et al. 2013](#)), accretion-induced collapse (AIC) has been proposed as an alternative fate of WDs approaching M_{Ch} ([Nomoto & Kondo 1991](#)). Massive oxygen-neon-magnesium (ONeMg) WDs left behind by intermediate-mass stars ($8 - 9 M_{\odot}$) are thought to follow this pathway more probably ([Schwab et al. 2017](#)). Though not confirmed in electromagnetic observations yet, AIC has several important theoretical and observational implications. Compared to core-collapse supernovae (CCSNe) of massive stars ($M \gtrsim 10 M_{\odot}$), AICs leave behind remnant NSs with a lower baryonic mass ($\sim 1.35 M_{\odot}$) as the progenitor WDs weigh $M_{\text{Ch}} \sim 1.44 M_{\odot}$ at most, ignoring rotational effects. These NSs can be the low-mass branch pulsars found in the bimodal NS mass distribution ([Schwab et al. 2010](#); [Özel et al. 2012](#); [Farrow et al. 2019](#)). AICs have interesting nucleosynthesis patterns and may contribute to the production of silver, palladium ([Hansen et al. 2012](#)), and some r-process elements ([Fryer et al. 1999](#); [Jones et al. 2019](#)). Due to the thin envelop and weak explosion energy ($\lesssim 10^{50}$ erg), AICs exhibit themselves as short and faint transients in electromagnetic waves, while they can emit strong X-ray flashes lasting ~ 1 hr in binary systems ([Piro & Thompson 2014](#)). A natural question is how DM admixture will change the evolution and outcomes of AIC.

To approach M_{Ch} , the progenitor WD accretes mass and angular momentum from its companion, and so rotation is an important ingredient of SNe Ia and AICs. [Fink et al. \(2018\)](#) pointed out that thermonuclear explosions of rapidly rotating WDs can be candidates for superluminous SNe Ia. The collapses of rotating stars, including AICs, are expected to emit strong bursts of gravitational waves (GW) ([Ott 2009](#)). They are among the potential targets for ground-based GW detectors such as LIGO ¹, Virgo, ², KAGRA ³, and the third generation detector Einstein Telescope ([Hild et al. 2011](#)). Due to the complicated nature of the collapse and bounce dynamics, there is no analytic solution for the GW waveforms for rotating AICs, which are indispensable for

powerful data analysis algorithms such as matched filtering ([Gossan et al. 2016](#)). Accurate waveforms can only be calculated from computationally demanding hydrodynamical simulations. Because AICs emit transients of optical photons ([Piro & Thompson 2014](#)), radio-waves ([Piro & Kulkarni 2013](#)), neutrinos ([Dessart et al. 2006](#)) and GWs, they are interesting candidates in the new era of multi-messenger astronomy. An extended question is how these observations can tell us whether DM is admixed in the progenitor or not.

In paper I ([Leung et al. 2019, in prep.](#)), we performed spherically symmetric simulations and found that DM admixed AICs produce light NSs with mass compatible with that of the recently observed low mass (baryonic mass $\sim 1.28 M_{\odot}$) NS in the binary system PSR J0453+1559 ([Martinez et al. 2015](#)). In this paper, we examine the AIC dynamics and GW signals when the rotating progenitor WD bears a DM core of different masses, with axisymmetric hydrodynamical simulations. Specifically, we check whether the presence of DM can be identified through the GW observations.

This paper is organized as follows. Section 2 introduces the methods for constructing initial models, the subsequent hydrodynamical simulations and extraction of GW waveforms. Section 3 presents the results of AIC simulations, focusing on the dependence of the dynamics and emitted GWs on both rotation rate and M_{DM} . We discuss how to break the degeneracy of GWs on rotation rate and M_{DM} and retrieve parameters with a quantitative analysis of the extracted GW waveforms. In Section 4, we compare the difference between this work and a previous study without DM admixture ([Abdikamalov et al. 2010](#)). We also discuss the possible observational implications on the proto-neutron star (PNS) g-mode GW emission. We summarize our results in Section 5.

2. METHODS

We performed axisymmetric simulations of AIC starting from a rotating WD with various M_{DM} , using the Newtonian hydrodynamical code developed in [Leung et al. \(2015b\)](#). The code has been used to model SNe Ia ([Leung et al. 2015a](#); [Leung & Nomoto 2018, 2019](#)) and electron capture supernovae ([Leung et al. 2019](#)), and we implemented necessary physics modules for modeling AIC and extracting GW waveforms. This section outlines the essence of the methods used in this paper.

2.1. Initial models

We followed [Hachisu \(1986\)](#) to generate the rotating WD self-consistently as the initial model for the hydrodynamical simulations. In this method, the equation of

¹ www.ligo.org/

² public.virgo-gw.eu/

³ gwcenter.icrr.u-tokyo.ac.jp

rotational equilibrium is given by

$$H(\rho) \equiv \int \rho^{-1} dP = C - \Phi + \int \Omega^2 \varpi d\varpi. \quad (1)$$

Here, ρ and P are the density and pressure of baryonic normal matter (NM), C the constant of integration, Φ the gravitational potential, ϖ the perpendicular distance from the axis of rotation and Ω the angular velocity at ϖ . This integral equation is solved iteratively until the constant C and stellar mass M converge. The equation of state (EOS) of NM ($P = P(\rho)$) is the ideal degenerate electron gas EOS with an electron fraction $Y_e = 0.5$. The extra gravity provided by the DM is described in the Poisson equation by including the DM density (ρ_{DM})

$$\nabla^2 \Phi = 4\pi G(\rho + \rho_{\text{DM}}). \quad (2)$$

The DM admixture is assumed to be non-rotating for simplicity and its structure together with non-rotating NM is initially solved by a spherically-symmetric two-fluid hydrostatic equation (Leung et al. 2015a)

$$\begin{aligned} \frac{dP}{dr} &= -\frac{G(M(r) + M_{\text{DM}}(r))}{r^2} \rho, \\ \frac{dP_{\text{DM}}}{dr} &= -\frac{G(M(r) + M_{\text{DM}}(r))}{r^2} \rho_{\text{DM}}, \end{aligned} \quad (3)$$

where P_{DM} is the pressure of DM calculated according to the DM model described below. $M(r)$ and $M_{\text{DM}}(r)$ are the enclosed masses of NM and DM, respectively, at radius r calculated by

$$\begin{aligned} \frac{dM(r)}{dr} &= 4\pi r^2 \rho, \\ \frac{dM_{\text{DM}}(r)}{dr} &= 4\pi r^2 \rho_{\text{DM}}. \end{aligned} \quad (4)$$

The DM density profile ρ_{DM} is then fixed during the iteration process of solving Eqs. 1 and 2.⁴

Since the properties of DM are very uncertain (Bertone & Hooper 2018), as the first example in studying its effects on AIC, DM particles are assumed to be ideal Fermions with particle mass 1 GeV without any self-annihilation or self-interaction (Xiang et al. 2014; Kouvaris & Nielsen 2015; Leung et al. 2015a; Mukhopadhyay & Schaffner-Bielich 2016; Cermeño et al. 2017). The choice of particle mass 1 GeV is consistent with a recent proposal that the mass of DM particle is less than a few GeV (Barkana 2018) in order to explain the amplitude of the 21-centimeter signal from hydrogen

⁴ We found that the change in ρ_{NM} within the size of DM admixture is $\mathcal{O}(10^{-3})$.

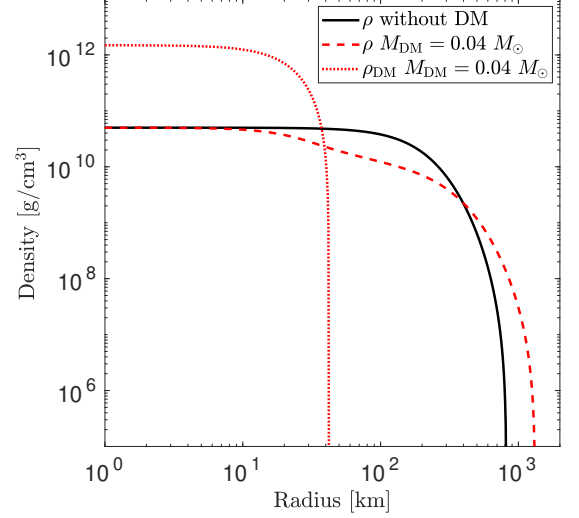


Figure 1. Density profiles of NM and DM for two non-rotating WD models. The black solid line is the NM density profile for the WD without DM admixture. The red dashed and dotted lines are the NM and DM density profiles, respectively, for the WD with $0.04 M_{\odot}$ of DM admixture.

atoms in the very early universe detected by EDGES (Bowman et al. 2018).

The rotation law for AIC or SN Ia progenitors is uncertain and depends on how the WD grows to M_{Ch} (Yoon & Langer 2004; Abdikamalov et al. 2010). Also, the central density for an AIC progenitor is not accurately determined from stellar evolution calculation yet (Schwab et al. 2017; Schwab & Rocha 2019), but it must lie in a narrow range for the gravitational instability to trigger the collapse. As we are focusing on the effects of DM admixture on AIC, as a first step only uniformly rotating progenitors (the angular velocity Ω is constant throughout the WD) are considered with a fixed central density of $5 \times 10^{10} \text{ g/cm}^3$, which is a value commonly used in hydrodynamical simulations of AIC (Dessart et al. 2006; Abdikamalov et al. 2010) and close to the value $\sim 4 \times 10^{10} \text{ g/cm}^3$ for ONeMg core collapse (Kitauro et al. 2006). We have used other central densities to verify that its exact value does not affect our conclusion on the DM effects in Appendix C, and we leave differential rotation for a future study.

Firstly, in Fig. 1 we plot the density profiles of NM and DM for two non-rotating WD models, without DM and with DM admixture of $0.04 M_{\odot}$. For the DM admixed model, DM resides in the central region as a compact core, with a radius of $\sim 40 \text{ km}$. The lower limit for integrating M_{DM} is taken to be 10^4 g/cm^3 . The exact value of this lower limit does not significantly affect M_{DM} as the DM density drops steeply at $\rho_{\text{DM}} \lesssim 10^9 \text{ g/cm}^3$. As the DM core provides additional gravitational pull to NM, the NM density decreases more quickly compared

to the model without DM admixture. However, the WD becomes more extended due to the smaller total mass of the hybrid star, including NM and DM.

The global properties of 1 GeV fermionic DM admixed rotating WDs with the same initial angular velocity ($\Omega_{\text{ini}} = 5$ rad/s, near the Keplerian limit for $M_{\text{DM}} = 0.04 M_{\odot}$) are summarized in Table 1. Admixture of DM makes the star more extended in radial size but less massive, and increases the ratio between the rotational kinetic and gravitational binding energies ($\beta \equiv E_{\text{Rot}}/|E_{\text{Grav}}|$). The total masses, M_{WD} (including NM and DM), and initial values of the β parameter, β_{ini} , for all the constructed WDs are plotted in Fig. 2. For slow rotation ($\beta_{\text{ini}} \lesssim 0.7\%$), β_{ini} can be approximated by a quadratic function of the initial angular speed Ω_{ini} ($\beta_{\text{ini}} \propto \Omega_{\text{ini}}^2 [R_{\text{WD}}^{(0)}]^3 / M_{\text{WD}}^{(0)}$), where $R_{\text{WD}}^{(0)}$ and $M_{\text{WD}}^{(0)}$ are the radius and mass of a non-rotating WD for each M_{DM} (a superscript (0) stands for non-rotating case throughout this paper). The Keplerian velocity is decreased from ~ 10.9 rad/s without DM admixture to ~ 5 rad/s for $M_{\text{DM}} = 0.04 M_{\odot}$, due to the more extended radius. Limited by the Keplerian limit, the maximum β_{ini} is $\sim 1.33\%$ for all our models, regardless of the amount of DM admixture. The initial WD mass is increased by at most $0.06 M_{\odot}$ in the near-Keplerian rotation case, while it is decreased when DM is admixed, by $0.2 M_{\odot}$ for $M_{\text{DM}} = 0.04 M_{\odot}$. The increment of M_{WD} due to rotation can be parametrized by

$$M_{\text{WD}} = [1 + (3.04 \pm 0.02) \times \beta_{\text{ini}}] M_{\text{WD}}^{(0)}, \quad (5)$$

where $M_{\text{WD}}^{(0)}$ is 1.44, 1.41, 1.37, 1.33, 1.28 M_{\odot} for $M_{\text{DM}} = 0, 0.01, 0.02, 0.03, \text{ and } 0.04 M_{\odot}$, respectively.

2.2. Hydrodynamics

To follow the collapse of a white dwarf to PNS and the subsequent bounce and post-bounce dynamics, we solve the two-dimensional Euler equations of NM assuming axisymmetry (Leung et al. 2015b):

$$\begin{aligned} \partial_t \rho + \nabla \cdot (\rho \vec{v}) &= 0, \\ \partial_t (\rho \vec{v}) + \nabla \cdot (\rho \vec{v} \vec{v}) + \nabla P &= -\rho \nabla \Phi, \\ \partial_t (\tau) + \nabla \cdot [(\tau + P) \vec{v}] &= -\rho \vec{v} \cdot \nabla \Phi. \end{aligned} \quad (6)$$

Here $\tau = \rho(\epsilon + \frac{1}{2}v^2)$ is the total energy density, where ϵ is the specific internal energy and \vec{v} is the fluid velocity. Our code utilizes a fifth-order shock capturing scheme Weighted-Essentially-Non-Oscillation (WENO; Liu et al. 1994) for the spatial discretization and 5-stage third-order Runge-Kutta scheme for time integration. As a first step, the DM admixture is assumed stationary and affects the dynamics of NM only through its gravity. The dynamics of DM accompanying AIC is an interesting problem and will be our future work. We used a

grid setup similar to that employed by the FORNAX code (Skinner et al. 2016), which has a uniform resolution of 370 m in the central 70 km and becomes logarithmically increasing in the outer part (~ 5 km near the WD surface), and 45 angular grids are used in the quarter from the polar to equatorial planes. Simulations with finer resolutions in both radial and angular directions were performed and showed convergent results of the GW waveforms (Appendix D). The hydrodynamic equations need to be closed with a gravity solver for Φ and EOS, which together with other microphysics inputs are described in the remaining part of this section.

In our Newtonian hydrodynamics modeling, we mimic the relativistic gravity effects by modifying Φ and its derivative following the Case A formula presented in Marek et al. (2006), which has been shown to give reasonable agreements of the central density evolution and GW waveform compared to general relativistic (GR) simulations (CFC+ approximation, Dimmelmeyer et al. 2002) for slowly rotating CCSNe. This implementation is widely used in many recent CCSN simulations (e.g. Vartanyan et al. 2019), even in the cases of black hole formation and failed supernovae (Pan et al. 2018).

There are still large uncertainties in the nuclear matter EOS at high density for modeling CCSNe and NSs (Oertel et al. 2017). It has been explored extensively in Richers et al. (2017) for CCSN simulations, and we have tested the difference in results for AIC without DM admixture using 3 typical EOSs in Appendix B. The EOS provided by Lattimer & Swesty (1991) with compressibility $K = 220$ MeV (LS220) is selected for NM for our discussion on the differences between AICs with different M_{DM} . This choice is mainly because LS220 has been widely used in many CCSN simulations and it agrees reasonably well with nuclear experiments and the measured masses and radii of NSs. Particularly, LS220 was used in several recent studies of GW signals from CCSNe with multi-dimensional simulations (e.g. Cerdá-Durán et al. 2013; Morozova et al. 2018; Andresen et al. 2019). To use the finite temperature EOSs, we impose the same parameterized temperature profile to the initial models as Dessart et al. (2006)

$$T = T_c [\rho / \rho_{c,\text{ini}}]^{0.35}, \quad (7)$$

where the initial central temperature T_c is set to be 5 GK.

To trigger and follow the collapse of WDs, we use the parametrized electron capture scheme (Liebendörfer 2005), in which Y_e is a function of NM density before the core bounce and neutrino pressure is included only in the trapping regime ($\rho > 2 \times 10^{12}$ g/cm³). The $\rho - Y_e$ relation is obtained from the central trajectory

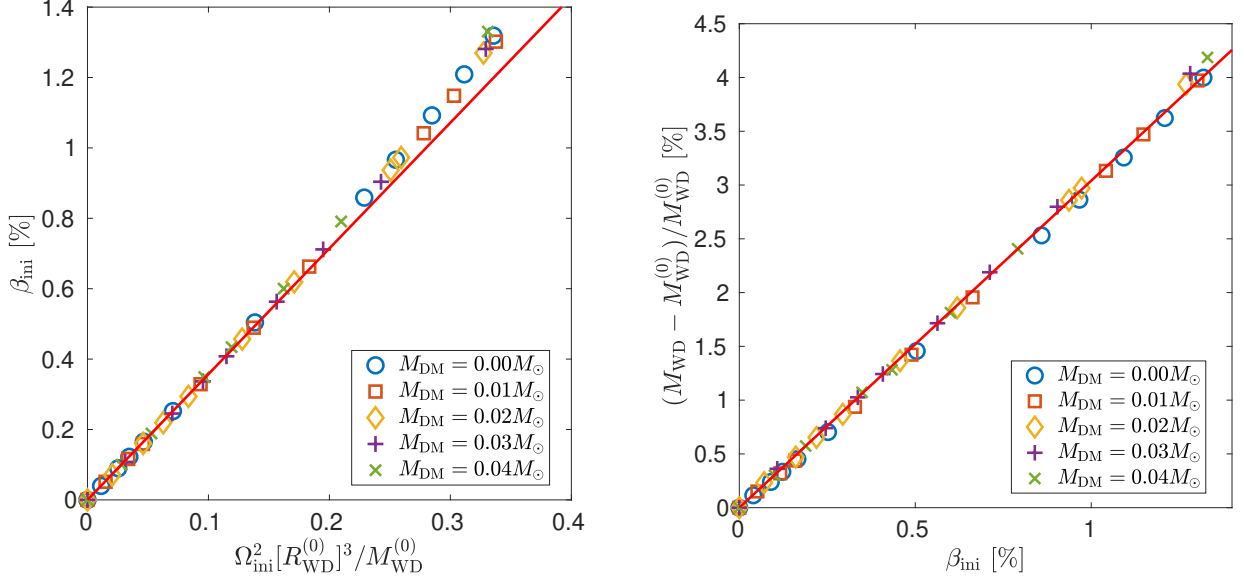


Figure 2. β_{ini} (left) and fractional increment of M_{WD} relative to $M_{\text{WD}}^{(0)}$ in the non-rotating case (right) for the initial rotating WDs, with different M_{DM} . β_{ini} shows a quadratic relation with Ω_{ini} for slow rotation ($\beta_{\text{ini}} \lesssim 0.7\%$) and is proportional to the relative increment of M_{WD} .

Table 1. Global parameters of DM admixed rotating WDs.

Model	$M_{\text{DM}} [M_{\odot}]$	$M_{\text{NM}} [M_{\odot}]$	$J [10^{50} \text{erg} \cdot \text{s}]$	$\beta_{\text{ini}} [\%]$	$R_{\text{e}} [\text{km}]$	$R_{\text{p}}/R_{\text{e}}$
R5-DM0	0	1.458	0.09	0.25	849	0.956
R5-DM1	0.01	1.416	0.11	0.33	934	0.942
R5-DM2	0.02	1.374	0.13	0.46	1043	0.928
R5-DM3	0.03	1.333	0.16	0.71	1243	0.896
R5-DM4	0.04	1.303	0.25	1.33	1809	0.726

NOTE—All models have a central baryonic matter density of $5 \times 10^{10} \text{ g/cm}^3$ and initial angular velocity of 5 rad/s. M_{DM} and M_{NM} are the masses of dark matter and baryonic matter components; J is the total angular momentum; β_{ini} is the initial ratio of rotational energy to gravitational energy; R_{e} and R_{p} are the equatorial and polar radii of the white dwarfs, respectively. We extend this table to all our models in Tables E1 and E2 of Appendix E.

of a spherically symmetric simulation of AIC with the open-source code GR1D (O’Connor 2015), which has included a two-moment neutrino transport scheme and all the important emission and scattering reactions between neutrinos and NM.⁵ Some important GR1D results are presented in Appendix A. After the core bounce, no further deleptonization is included and Y_{e} is simply advected. Since the post-bounce phase is evolved without neutrino transport, we present results mostly in the early post-bounce phase ($\lesssim 15$ ms after bounce) during

⁵ We used Newtonian hydrodynamics with the effective GR potential in the GR1D simulation. The ρ – Y_{e} relation is not affected by different treatments of the GR effect.

which neutrino leakage has a very small effect on the evolution (Ott et al. 2012).

2.3. Extraction of gravitational waves

For our Newtonian hydrodynamical simulations, we utilize the standard quadrupole formula in the slow-motion and weak-field approximations to extract the GW strain h_{+} from the simulations (Moenchmeyer et al. 1991)

$$h_{+} = \frac{3}{2} \frac{G}{Dc^4} \ddot{I}_{\text{zz}} \sin^2 \theta, \quad (8)$$

where the source is placed at a distance of D and orientation angle of θ , and \ddot{I}_{zz} is the second time derivative of the mass-density quadrupole moment. While there are variants for performing the time derivative to minimize numerical noise (Finn & Evans 1990), we found

convergence among them by improving the accuracy of integration and optimizing the recording time-steps.

3. RESULTS

In this section, we present the major results from our hydrodynamical simulations of AIC of DM admixed rotating WDs. Section 3.1 describes how DM affects the collapse dynamics and properties of the inner core at the time of bounce (t_b). Then we present the waveforms of the emitted GWs with various rotational speeds and M_{DM} , as well as the detection prospect in Section 3.2. In Section 3.3, we further analyze the GW signals and dig out the imprinted information, especially on how to break the degeneracy between M_{DM} and the rotation rate.

3.1. Dynamics

AIC without DM admixture has been studied assuming spherical symmetry (Fryer et al. 1999) and axisymmetry (Dessart et al. 2006; Abdikamalov et al. 2010), and we summarize the essential features of its dynamics here. A WD is supported by electron degeneracy pressure, and when it reaches the effective M_{Ch} this pressure support is reduced as electrons with high Fermi energy are captured by nuclei. The subsequent temporal evolution (Fig. 3) can be divided into 3 phases similar to the canonical CCSNe (Janka 2012): infall, plunge and bounce, and ringdown. During the infall phase, ρ_c rises slowly and the WD is separated into two parts, a homologously collapsing inner core ($v_r \propto r$) and a supersonically collapsing outer core, which are in loose contact with each other. As ρ_c rises to above the nuclear saturation density ($\rho_{\text{sat}} \simeq 2.7 \times 10^{14} \text{ g/cm}^3$), the inner core overshoots its equilibrium configuration and then sends out a hydrodynamic bounce shock, which turns into an accretion shock as its kinetic energy is lost due to disintegration of heavy nuclei and neutrino emissions (Janka 2012). Following Liebendörfer (2005), the bounce time t_b is defined to be the instant when entropy per baryon at the edge of the inner core exceeds $3 k_B$, which signifies the launch of the bounce shock.

Fig. 3 shows the ρ_c evolution for the models listed in Table 1. In the early infall phase, as the central gravitational potential well is deeper for a larger M_{DM} , models with more admixed DM show a faster contraction during the first ~ 5 ms (left panel of Fig. 3). But as DM admixture decreases M_{WD} and enlarges its size, the surge of ρ_c and bounce time t_b are delayed, and the central density at t_b , $\rho_{c,b}$, is decreased for a larger M_{DM} (right panel of Fig. 3). These effects are qualitatively the same as found in non-rotating models (Leung et al. 2019, in prep.).

Faster rotation also delays the plunge and bounce phase, as well as decreases ρ_c through the centrifu-

Table 2. Parameters of the non-rotating models

Model	M_{DM}	$t_b^{(0)}$	$\rho_{c,b}^{(0)}$	$M_{\text{ic,b}}^{(0)}$	$M_{\text{PNS}}^{(0)}$
	$[M_\odot]$	[ms]	$[10^{14} \text{ g/cm}^3]$	$[M_\odot]$	$[M_\odot]$
R0-DM0	0	32.8	3.99	0.558	1.26
R0-DM1	0.01	37.7	3.90	0.543	1.21
R0-DM2	0.02	45.2	3.80	0.528	1.15
R0-DM3	0.03	58.6	3.69	0.510	1.07
R0-DM4	0.04	86.1	3.55	0.490	0.99

NOTE—The superscript (0) denotes non-rotating models. We extend this table to all our models in Tables E1 and E2 of Appendix E.

gal support. The β parameter of the inner core at t_b , $\beta_{\text{ic,b}}$, is generally used as a measure for its rotation rate, and is found to strongly correlate with the emitted GW amplitude (Dimmelmeier et al. 2008; Abdikamalov et al. 2010). In Fig. 4, $\beta_{\text{ic,b}}$ is plotted as a function of the initial angular velocity Ω_{ini} for different M_{DM} . Interestingly, $\beta_{\text{ic,b}}$ shows a power-law relation to Ω_{ini} ($\beta_{\text{ic,b}} = C_b \Omega_{\text{ini}}^\alpha$) with an exponent α less than 2 that weakly depends on M_{DM} (the red lines in Fig. 4) despite the highly nonlinear dynamical processes. The maximum value of $\beta_{\text{ic,b}}$ is $\approx 9\%$ for $M_{\text{DM}} = 0.04 M_\odot$. This is below $\beta_{\text{dyn}} \simeq 0.25$ for developing the dynamical high- β non-axisymmetric instability (Baiotti et al. 2007), while the elusive low- β instability may still develop in full three-dimensional simulations (see, e.g. Cerdá-Durán et al. 2007). In this work, we only consider axisymmetric modeling.

To disentangle the effects of DM admixture and rotation on the dynamics, we define the relative differences of a parameter \mathcal{O} , between the rotating and non-rotating models with the same M_{DM} as:

$$\Delta[\mathcal{O}] \equiv (\mathcal{O} - \mathcal{O}^{(0)})/\mathcal{O}^{(0)}, \quad (9)$$

where $\mathcal{O}^{(0)}$ is for the non-rotating models. $\Delta[t_b]$ and $\Delta[\rho_{c,b}]$ are plotted as a function of $\beta_{\text{ic,b}}$ in Fig. 5. It is clear that these relative differences are proportional to $\beta_{\text{ic,b}}$ and have almost no explicit dependence on M_{DM} , up to around $\beta_{\text{ic,b}} \approx 6\%$ (red lines in both panels of Fig. 5). The offsets of t_b and $\rho_{c,b}$ due to DM admixture can be calculated from the non-rotating models listed in Table 2. Despite the decrease of $\rho_{c,b}$ for a larger M_{DM} and $\beta_{\text{ic,b}}$, all the models bounce at $\rho_{c,b} > \rho_{\text{sat}}$. This suggests that the uniform rotation of the progenitor WDs considered here is not too fast to result in a centrifugal bounce (Dimmelmeier et al. 2008).

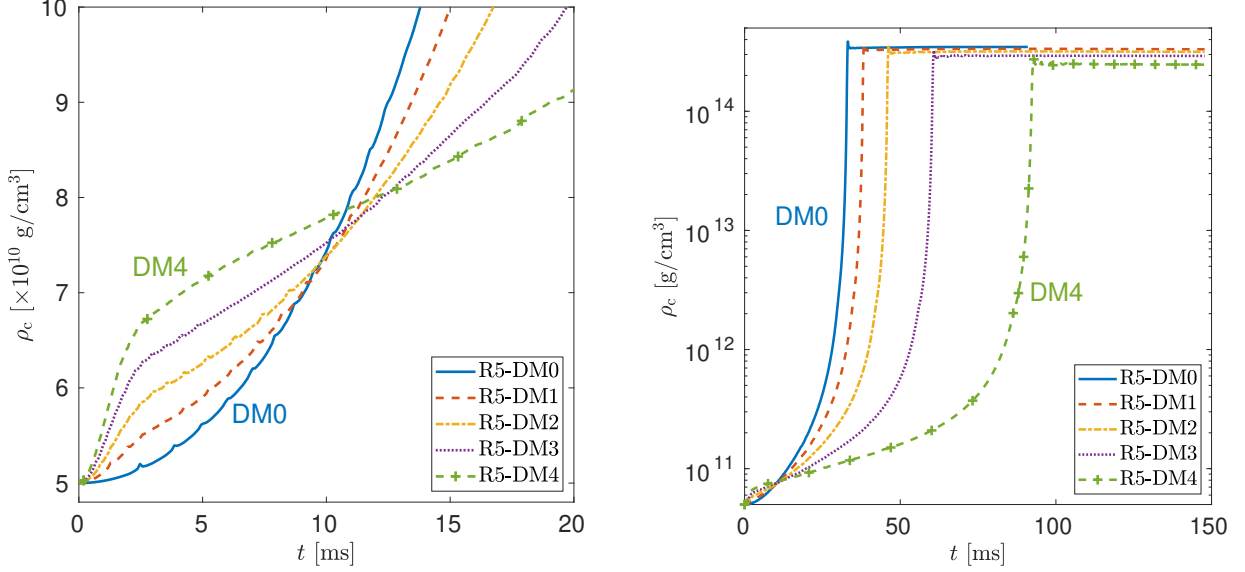


Figure 3. Central density evolution for the first 20 ms (left) and entire time interval (right) of AIC simulations starting from models listed in Table 1.

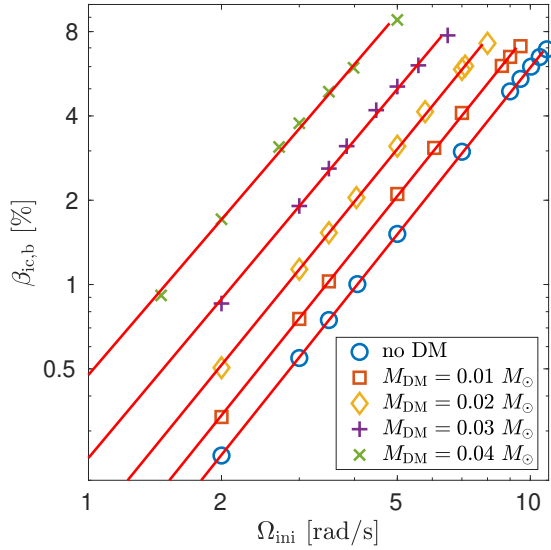


Figure 4. The β parameter of the inner core at t_b , $\beta_{ic,b}$, as a function of Ω_{ini} for different M_{DM} .

The mass of the inner core at the bounce, $M_{ic,b}$, is another important parameter for AIC, which affects the strength of the bounce shock and also correlates with the GW amplitude. As listed in Table 2, $M_{ic,b}^{(0)}$ decreases with increasing M_{DM} , in accordance with the smaller $M_{WD}^{(0)}$ and $\rho_{ic,b}^{(0)}$. $\Delta[M_{ic,b}]$ increases linearly with $\beta_{ic,b}$, and the increasing slope is smaller for a larger M_{DM} . Fig. 6 shows the rescaled $\Delta[M_{ic,b}]$ as a function of $\beta_{ic,b}$, which demonstrates their linear correlation

$$\Delta[M_{ic,b}]/\alpha(M_{DM}) = (1.71 \pm 0.02) \times \beta_{ic,b}, \quad (10)$$

where the denominator:

$$\alpha(M_{DM}) = 3.24 - [1 - 11.6(M_{DM}/M_{\odot})]^{-1}, \quad (11)$$

takes into account the M_{DM} dependence. This equation will be used in Section 3.3 for inferring M_{DM} from the GW amplitudes.

3.2. Gravitational waves

Rotating stellar collapses are expected to emit strong burst GWs and have been investigated for decades (see the review by Ott (2009)). Detailed hydrodynamical simulations of rotating CCSNe (Dimmelmeier et al. 2008) and AICs (Abdikamalov et al. 2010) have shown that they emit GWs with generic waveforms. Here we study the dependence of the GW waveform on a new degree of freedom, M_{DM} .

Firstly, the GW waveforms of 3 normal rotating AIC models ($M_{DM} = 0$) are given in Fig. 7. They represent our slowest, moderately, and fastest rotating WD models. The waveform type is different from that in Abdikamalov et al. (2010) according to the classification in Ott (2009), and this will be discussed in Section 4.1. Similar to the CCSNe (Dimmelmeier et al. 2008), the waveforms from AIC models in this study are Type I (pronounced spikes around t_b associated with core bounce induced by stiffening of the nuclear EOS, followed by “ring-down” oscillations) and can be divided into two sub-groups: the slow rotating models (upper panel in Fig. 7) show significant contributions from prompt convection after ~ 5 ms post-bounce as long period oscillations, while fast rotating models (middle and lower panels in Fig. 7) show dominantly

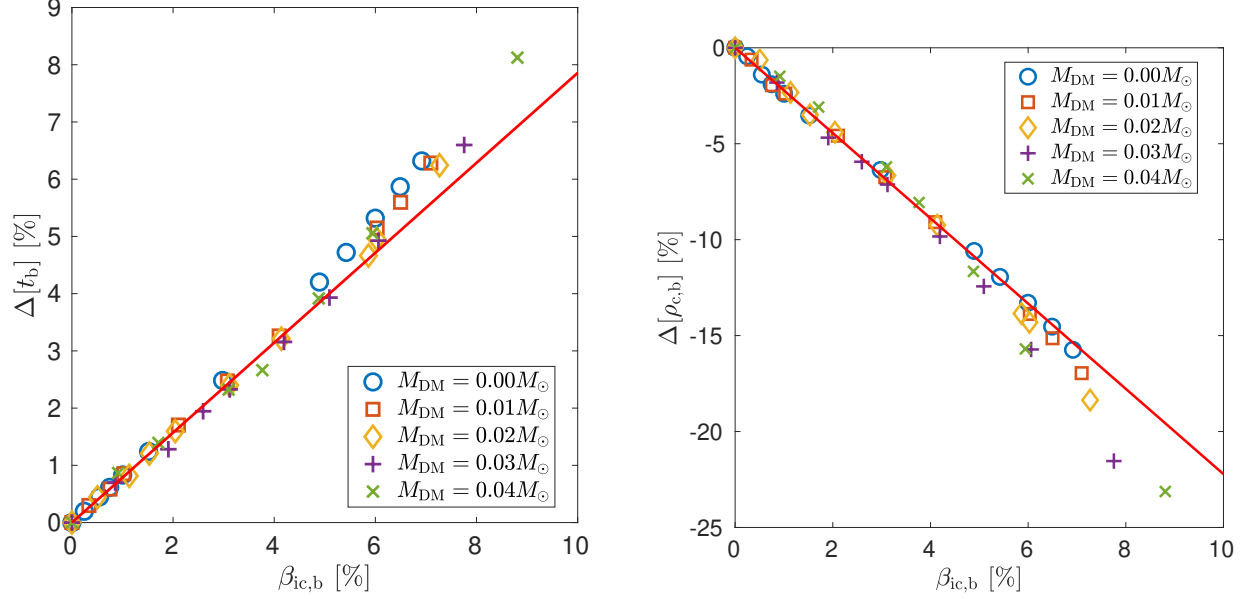


Figure 5. Relative differences of t_b (left) and $\rho_{c,b}$ (right) between the rotating and non-rotating models with the same M_{DM} as a function of $\beta_{ic,b}$.

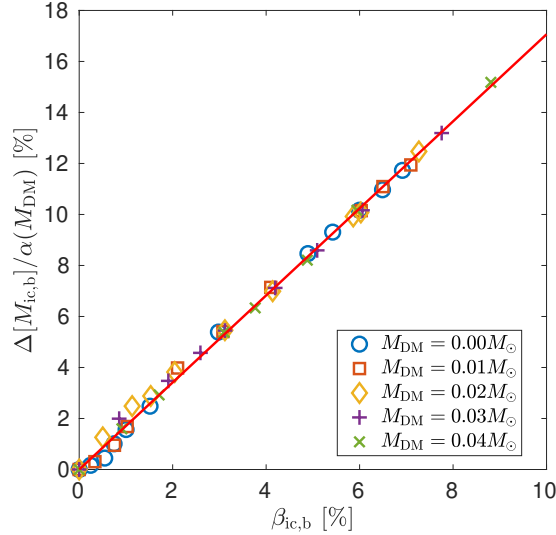


Figure 6. Same as Fig. 5, but for the relative differences of $M_{ic,b}$ divided by $\alpha(M_{DM})$.

post-bounce ring-down signals only. None of our models displays centrifugal bounce since the maximum $\beta_{ic,b}$ is quite small ($< 9\%$), and $\rho_{c,b}$ is always above ρ_{sat} for the initial WDs with uniform rotation. In the middle panel of Fig. 7, the dashed and dotted curves are those in the upper and lower panels but multiplied by a constant factor. The excellent match of the spikes around t_b shows the genericity of the waveforms, and this feature will be further analyzed in Section 3.3.

We then show the waveforms from models with the same Ω_{ini} of 5 rad/s but different M_{DM} in Fig. 8. With DM admixture, the waveform shape still belongs to the

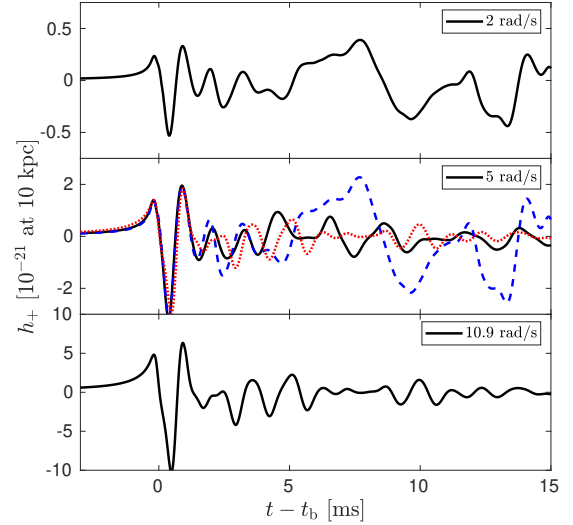


Figure 7. GW waveform of AIC without DM admixture starting for the slowest (upper panel), moderately (middle panel), and fastest (lower panel) rotating WDs. In the middle panel, the blue dashed (red dotted) curve is the same as the upper (lower) panel but multiplied with a constant factor, in order to illustrate the genericity of GW signals around t_b .

Type I category. For the same Ω_{ini} and ρ_c , a larger M_{DM} leads to a larger β_{ini} (Fig. 2) and $\beta_{ic,b}$ (Fig. 4). This results in some enhancement of the GW emission, especially amplitudes of the three spikes around the time of bounce.

Results in Dimmelmeier et al. (2008) and Abdikamalov et al. (2010) suggest that the GW amplitude has a strong correlation with $\beta_{ic,b}$, and so $\beta_{ic,b}$ can in principle be

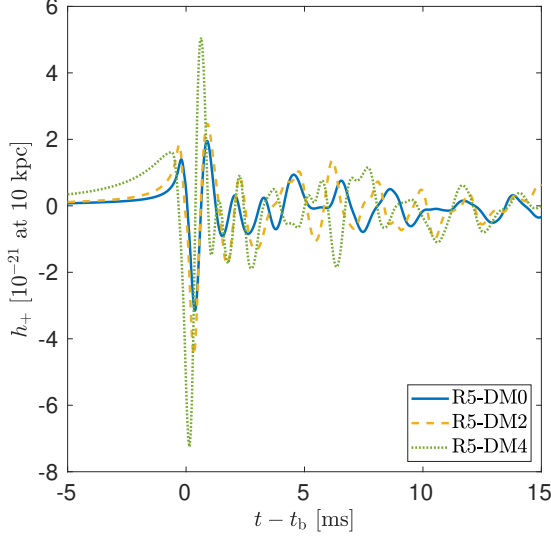


Figure 8. GW waveforms of AICs starting from DM admixed rotating WDs, with the same initial angular velocity $\Omega_{\text{ini}} = 5$ rad/s but different M_{DM} .

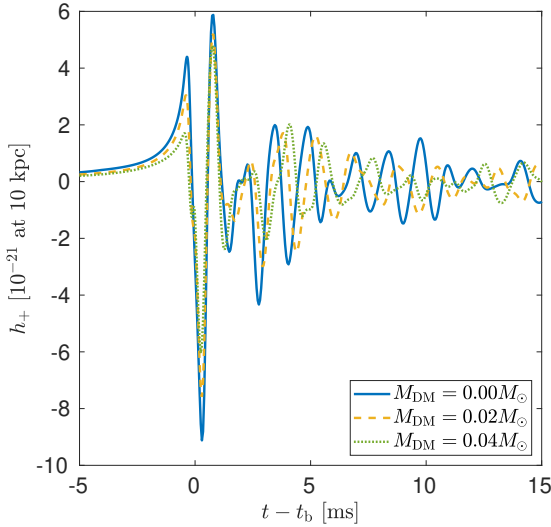


Figure 9. Same as Fig. 8, but for models with different M_{DM} but reaching the same $\beta_{\text{ic,b}} \sim 6\%$.

inferred from GW observations. In Fig. 9 we pick models with the same $\beta_{\text{ic,b}} (\simeq 6\%)$ but different M_{DM} . For this set of models, the GW amplitude around the bounce decreases significantly as M_{DM} increases. For example, the peak before the bounce decreases by 2.5 times for M_{DM} from 0 to $0.04 M_{\odot}$. This is related to the decrement of ρ_c (Fig. 5) and M_{ic} (Fig. 6), thus less compact core, for a larger M_{DM} . We will analyze these changes quantitatively in Section 3.3 to disentangle the effects of DM admixture and rotation rate.

For the detection prospect, the characteristic amplitude h_{char} of GWs from DM admixed AICs is compared

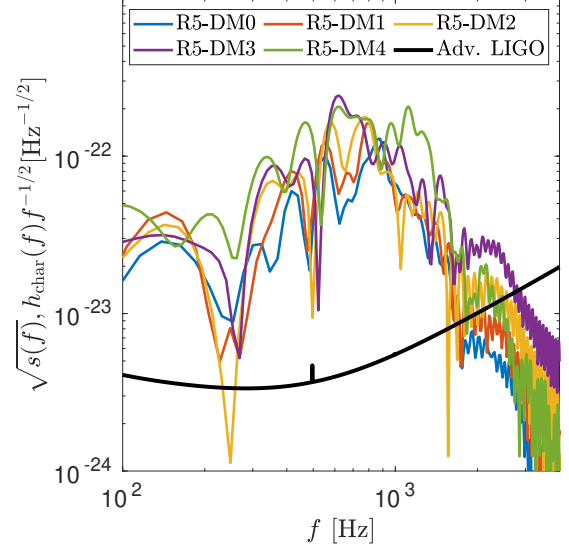


Figure 10. Characteristic strain spectra for selected models listed in Table 1 compared with the noise spectrum of Adv. LIGO. $\sqrt{s(f)}$ is the one-sided noise amplitude spectral density of a GW detector (black solid: LIGO noise curve, in file aLIGODesign.txt from Barsotti et al. 2018).

to the noise spectra of LIGO. Following Murphy et al. (2009), the dimensionless characteristic amplitude can be calculated by

$$h_{\text{char}} = \frac{1}{D} \sqrt{\frac{2G}{\pi^2 c^3} \frac{dE_{\text{GW}}}{df}}, \quad (12)$$

where $\frac{dE_{\text{GW}}}{df}$ is the GW spectral energy density,

$$\frac{dE_{\text{GW}}}{df} = \frac{4}{15} \frac{c^3}{G} (2\pi f)^2 D^2 |\tilde{h}_+|^2, \quad (13)$$

and \tilde{h}_+ is the Fourier transform of GW strain h_+

$$\tilde{h}_+(f) = \int_{-\infty}^{\infty} h_+(t) e^{-2\pi i f t} dt. \quad (14)$$

The Fourier transform includes signals only until 10 ms post-bounce to avoid possible contribution from prompt convection, and the h_{char} spectra of selected AIC models with different M_{DM} listed in Table 1 are plotted in Fig. 10, assuming that the AIC events are happening at 10 kpc (within the Milky Way) from the detectors. The GWs have a broad frequency contribution from ~ 200 Hz to ~ 1500 Hz and several peaks in-between, which lie in the most sensitive detection band of LIGO. However, from binary population synthesis calculations, the Galactic AIC rate is expected to be $10^{-4} - 10^{-3} \text{ yr}^{-1}$ summing over all possible progenitor scenarios (Wang 2018; Ruiter et al. 2019), which disfavors the detection of an AIC event. We estimated that with the proposed

sensitivity of the Einstein Telescope (Hild et al. 2011), the detection distance can be increased to ~ 1 Mpc, which will boost the detection possibility significantly.

3.3. DM imprints in GW

The GW waveforms shown in Fig. 7, 8 and 9 have three dominant spikes around t_b . We denote the amplitudes of these spikes as h_1 (positive, before t_b), h_2 (negative, after t_b) and h_3 (positive, after t_b). Previous studies (Richers et al. 2017) found that for CCSNe, h_1 and $\Delta h = h_1 - h_2$ increase monotonically with increasing $\beta_{ic,b}$ for $\beta_{ic,b} \leq 7\%$, and this correlation has relatively weak dependence on the EOS and differential rotation. For our DM admixed models, the amplitudes also depend on M_{DM} and so there is a degeneracy between the two parameters, M_{DM} and $\beta_{ic,b}$.

We plot the ratios of these peak amplitudes, i.e. h_2/h_1 and h_3/h_1 , as a function of $\beta_{ic,b}$ for different M_{DM} in Fig. 11. Without DM admixture, the two ratios have relatively small variations for different $\beta_{ic,b}$, with $h_2/h_1 = -2.14 \pm 0.14$ and $h_3/h_1 = 1.37 \pm 0.04$. DM admixture breaks down this invariance. The absolute values and variation of h_2/h_1 for different $\beta_{ic,b}$ are generally larger for a larger M_{DM} . For h_3/h_1 , the absolute value is smaller at $\beta_{ic,b} \lesssim 3\%$ and larger at $\beta_{ic,b} \gtrsim 4\%$ for a larger M_{DM} . For a fixed M_{DM} , h_3/h_1 is larger for faster rotation. Therefore, deviation of h_2/h_1 and h_3/h_1 from those of DM-absent models in a GW observation can indicate the presence of DM admixture. The relatively small spread of the ratios is also true for the CCSNe GW catalog provided by Richers et al. (2017) though the mean values of h_2/h_1 depend on the specific EOS and are between -2 and -3. The light shaded regions in Fig. 11 represent the uncertainties introduced by different EOSs simulated in Appendix B. If the DM core has a mass $M_{DM} \geq 0.03 M_\odot$, its existence can be inferred from the GW signals, despite our ignorance of the EOS. The presence of DM admixture with $M_{DM} \leq 0.02 M_\odot$ can be inferred only if the EOS is better constrained.

If a GW event of AIC is detected by a GW detector such as LIGO, can we infer the DM admixing? The mismatch (\mathcal{M}) between two GW waveforms for a given GW detector is (Reisswig & Pollney 2011; Richers et al. 2017)

$$\mathcal{M} = 1 - \max_{t_A} \left[\frac{\langle h_a, h_b \rangle}{\sqrt{\langle h_a, h_a \rangle \langle h_b, h_b \rangle}} \right], \quad (15)$$

where the second term is the match between the two waveforms h_a and h_b , maximized over the difference between their arrival times t_A . The inner product $\langle h_a, h_b \rangle$ is calculated by

$$\langle h_a, h_b \rangle = \int_0^\infty \frac{4\tilde{h}_a^* \tilde{h}_b}{s} df, \quad (16)$$

Table 4. Mismatches (\mathcal{M}) between the GW waveforms with the same $\beta_{ic,b}$, but without and with DM admixture. Both \mathcal{M} and $\beta_{ic,b}$ are in the unit of %.

	$\beta_{ic,b} \approx 1\%$		$\beta_{ic,b} \approx 3\%$		$\beta_{ic,b} \approx 6\%$	
$M_{DM} [M_\odot]$	$\beta_{ic,b}$	\mathcal{M}	$\beta_{ic,b}$	\mathcal{M}	$\beta_{ic,b}$	\mathcal{M}
0	1.00	0	2.98	0	6.00	0
0.01	1.03	8	3.08	7	6.03	5
0.02	1.13	14	3.12	20	6.03	19
0.03	0.86	39	3.12	31	6.06	34
0.04	0.91	35	3.10	39	5.94	47

where the Fourier spectrum \tilde{h} is defined in Eq. 14 and s is the noise spectrum of the LIGO detector (the black line in Figure 10). Here the integration limit is from 100 Hz to 2000 Hz, which is the dominant frequency range for the GW waveforms in this work.

In Table 4 we list the mismatches between the GW waveforms with the same $\beta_{ic,b}$ ($\approx 1\%$, 3% , 6%), but without and with DM admixture. Our results show that if the LIGO detector can distinguish two waveforms with $\mathcal{M} \gtrsim 10\%$, then the DM admixture with $M_{DM} \gtrsim 0.02 M_\odot$ can be inferred.

To retrieve the two parameters M_{DM} and $\beta_{ic,b}$ from a GW observation, we further analyze the dependence of $h_{1,2}$ on M_{DM} and $\beta_{ic,b}$ in Fig. 12. The dependence of h_1 on M_{DM} can be removed by rescaling it:

$$h_1^* \equiv h_1 / [1 - 15.36(M_{DM}/M_\odot)]. \quad (17)$$

For $\beta_{ic,b} \lesssim 7\%$, h_1^* follows a unified and monotonic increasing relation with $\beta_{ic,b}$. The analysis of h_2 is more subtle. We found that h_2 increases linearly with $\Delta[M_{ic,b}]$ (see Section 3.1 and Eq. 9 for the definition), which when rescaled by $\alpha(M_{DM})$ (Eq. 11) is proportional to $\beta_{ic,b}$ (Fig. 6). Therefore,

$$h_2^* \equiv \frac{h_2}{3.24 - [1 - 11.6(M_{DM}/M_\odot)]^{-1}} \quad (18)$$

also follows a unified and monotonic increasing relation with $\beta_{ic,b}$.

Using the universal relations, $h_1^*(\beta_{ic,b})$ and $h_2^*(\beta_{ic,b})$, in principle, M_{DM} and $\beta_{ic,b}$ can be retrieved from accurate measurement of $h_{1,2}$ in a GW observation. In addition, the whole waveform including the post-bounce ring-down oscillations can confirm this determination. One caution is that the microphysics inputs, such as $Y_e = Y_e(\rho)$ profile and EOS, may affect the exact functional forms of $h_{1,2}^*$. Fig. B1 shows that h_1 hardly changes for different EOSs while h_2 could change by $\sim 30\%$. Richers et al. (2017) showed that $\Delta h = h_1 - h_2$ varies by $\sim 30\%$ when the electron capture rate is scaled by 0.1 and 10. So a firm retrieval of M_{DM} awaits for better constrained microphysics inputs.

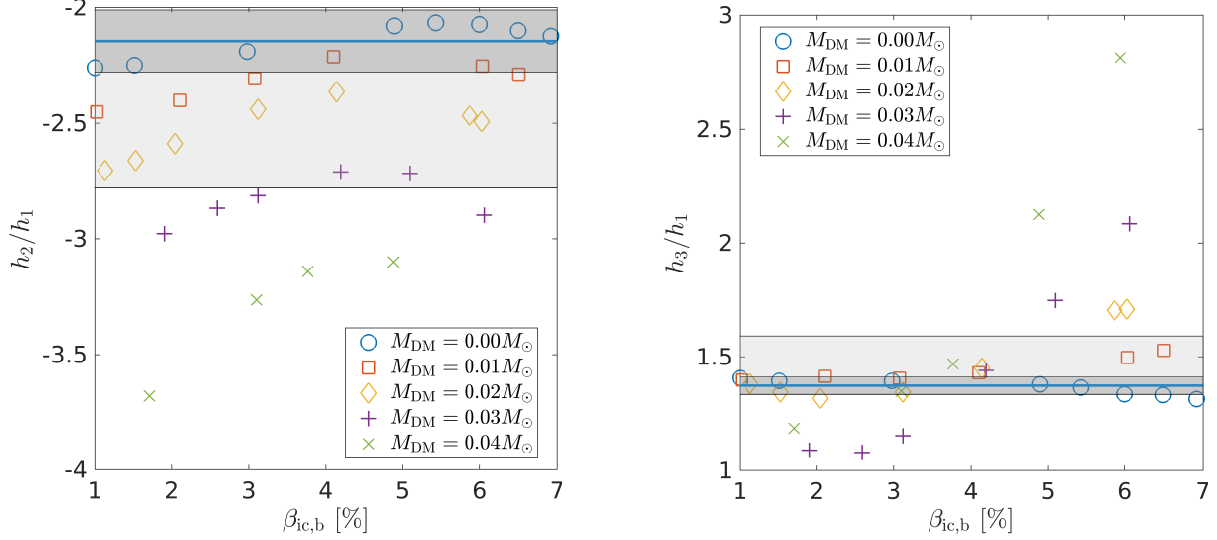


Figure 11. Ratios between the amplitudes of GW spikes ($h_{1,2,3}$ defined in the text) around t_b as a function of $\beta_{ic,b}$ for different M_{DM} . In both panels, the thick shaded region represents the variation due to different $\beta_{ic,b}$ and the light shaded region due to different EOSs.

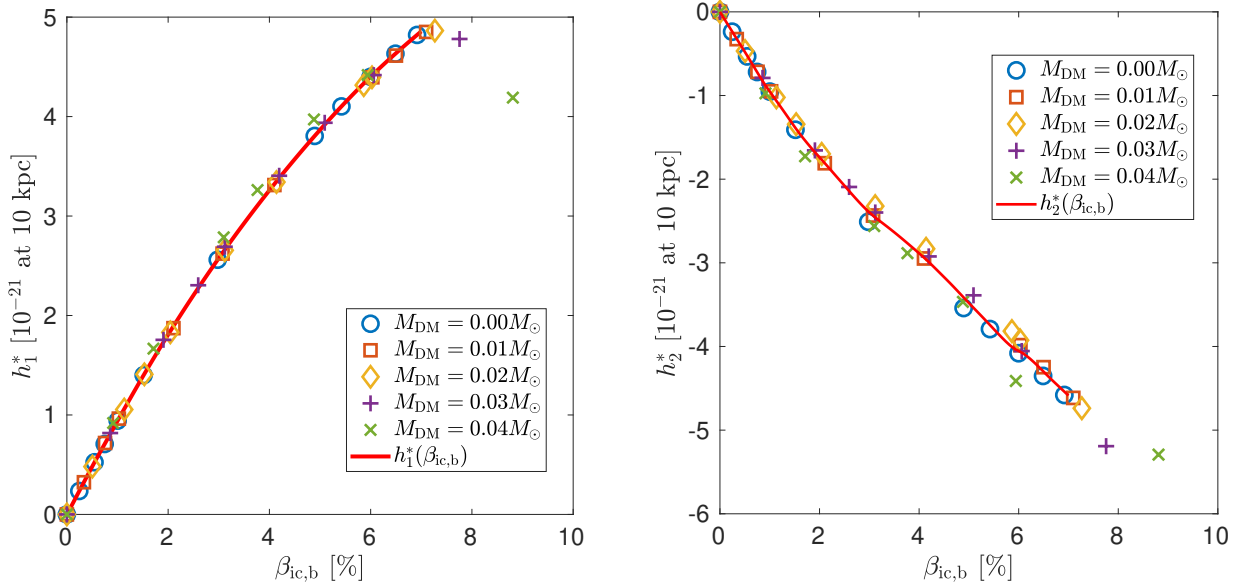


Figure 12. Same as Fig. 11, but for the rescaled values of $h_{1,2}$. The two red curves are interpolated from all the points at $\beta_{ic,b} \leq 7\%$ with the cubic spline method. The rescaling of $h_{1,2}$ are given by Eqs. 17 and 18, respectively.

4. DISCUSSION

4.1. Pre-bounce electron capture

Abdikamalov et al. (2010) has studied rotating AICs without DM admixture with general relativistic simulations using the CoCoNuT code (Dimmelmeier et al. 2002). They used the electron parametrization profile, $Y_e = Y_e(\rho)$, from AIC simulations with Multi-Group Flux-Limited Diffusion approximation for neutrino transport (Dessart et al. 2006), which resulted in

a very low central Y_e at the time of bounce (~ 0.19 compared to ~ 0.27 in simulations of CCSNe with more accurate neutrino transport schemes). The small central Y_e leads to a small mass of the homologous collapsing inner core ($M_{ic,b} \simeq 0.26 M_\odot$ for $\beta_{ic,b} \leq 10\%$) and a subdominant negative spike after bounce in GW emission, belonging to the Type III signal (Ott 2009). In our study, the parametrization profile obtained from GR1D simulations (Appendix A) is closer to those of standard

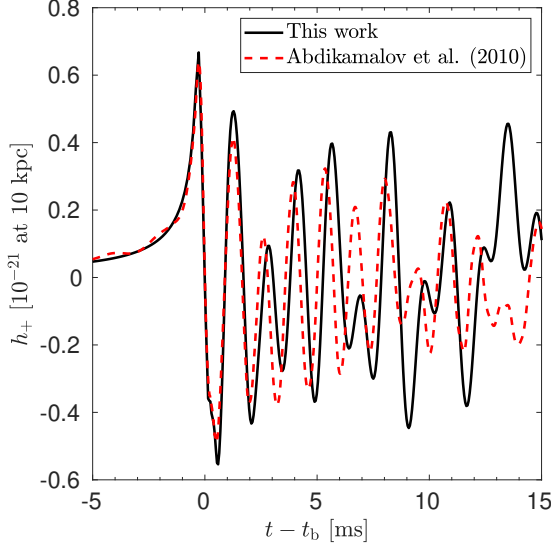


Figure 13. GW waveform (black solid line) from an AIC simulation with $\Omega_{\text{ini}} = 5$ rad/s and the same $Y_e = Y_e(\rho)$ profile as that used in Abdikamalov et al. (2010) compared with that from their GW catalog (red dashed line).

CCSNe. The presented GW waveforms in Figs. 7, 8 and 9 are generically Type I.

To check whether the different results obtained by us and Abdikamalov et al. (2010) are due to the microphysics employed or GR effect, we performed an AIC simulation with $\Omega_{\text{ini}} = 5$ rad/s and the same $Y_e = Y_e(\rho)$ profile as that used in Abdikamalov et al. (2010), and the GW waveform is shown in Fig. 13 compared to their result. The three spikes around t_b match quite well for the two waveforms, with $\sim 10\%$ difference in peak amplitudes. Our results agree with the study by Pajkos et al. (2019) who found a nearly identical bounce signal between CCSNe simulations with CoCoNuT and the Case A effective GR potential. The ring-down oscillations have different periods, which may be due to a discrepancy in the equilibrated PNS structure and/or grid resolution. As the numerical calculations of electron capture in the collapse phase is still uncertain (Nagakura et al. 2019), it would be interesting to study how this would generally affect our results. We hope to return to this issue in the future. Since our focus is the effects of DM admixture, the conclusions drawn from the bounce GW signals are expected not to be altered qualitatively.

4.2. PNS mass

Apart from the signal around t_b , the post-bounce convective motion inside and above the newborn PNS also emits significant GWs and is under intensive investigation recently in the context of CCSNe (e.g. Radice et al. 2019; Pajkos et al. 2019; Torres-Forné et al. 2019). An

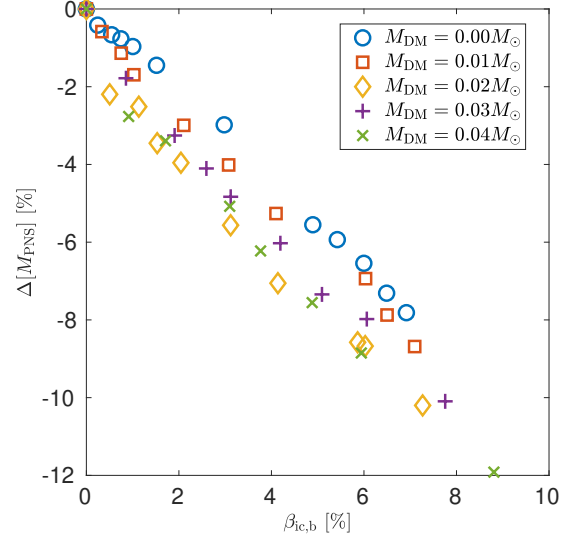


Figure 14. Same as Fig. 5, but for the relative differences of M_{PNS} defined in Section 4.2.

important emission mechanism is the g-mode oscillation at the surface of the PNS. Müller et al. (2013) found that the peak frequency of this g-mode GW is proportional to the PNS mass (M_{PNS}). We use M_{PNS} at 50 ms post-bounce to investigate the dependence of this signal on model parameters M_{DM} and $\beta_{\text{ic,b}}$, where the PNS is defined as the core with $\rho \geq 10^{11}$ g/cm³. Table 2 lists $M_{\text{PNS}}^{(0)}$ for the non-rotating models and it decreases from $1.26 M_{\odot}$ without admixed DM to $0.99 M_{\odot}$ for $M_{\text{DM}} = 0.04 M_{\odot}$. For a larger M_{DM} , the g-mode frequency is decreased by approximately $\sim 20\%$ for $M_{\text{DM}} = 0.04 M_{\odot}$, compared to that without DM admixture.

Faster rotation makes the PNS less compact and generally lighter through the centrifugal support. $\Delta[M_{\text{PNS}}]$ (defined in Eq. 9) are shown in Fig. 14 as a function of $\beta_{\text{ic,b}}$. M_{PNS} decreases linearly with increasing $\beta_{\text{ic,b}}$ and the decrement is $\sim 10\%$ at $\beta_{\text{ic,b}} \simeq 8\%$. DM admixture makes $\Delta[M_{\text{PNS}}]$ larger for the same $\beta_{\text{ic,b}}$, but this effect is not monotonic for increasing M_{DM} . The dependence of M_{PNS} and thus the g-mode frequency on both M_{DM} and $\beta_{\text{ic,b}}$ complements the relations found in Section 3.3, though the detailed frequency information awaits post-bounce neutrino transport simulations. A joint analysis of the bounce and PNS g-mode GW signals can unveil the presence of DM if admixed inside AICs.

5. CONCLUSION

We have performed axisymmetric hydrodynamical simulations of AIC of DM admixed WDs, with uniform rotation initially. With DM admixture, the early contraction is accelerated by the deeper central gravi-

tational potential well. However, the decrement of the total WD mass due to admixed DM eventually delays the plunge and bounce phase from ~ 30 ms for $M_{\text{DM}} = 0$ to ~ 100 ms for $M_{\text{DM}} = 0.04 M_{\odot}$. Also, the central density at bounce and equilibrium are smaller for a larger M_{DM} . Key characteristics for the collapse and bounce of AIC, \mathcal{O} , such as the bounce time and central density, generally depend on M_{DM} and $\beta_{\text{ic,b}}$, in a factorized form: $\mathcal{O} = f(\beta_{\text{ic,b}})\mathcal{O}^{(0)}(M_{\text{DM}})$, where $\mathcal{O}^{(0)}$ is for the non-rotating model with possible DM admixture.

The above results determine the dependence of GW signals during collapse and early post-bounce phases on $\beta_{\text{ic,b}}$ and M_{DM} . With the same Ω_{ini} and initial ρ_c , GW is enhanced by admixing DM. For models reaching the same $\beta_{\text{ic,b}}$, the GW amplitude is decreased by the DM admixture due to the less compact inner core. The ratios between GW amplitudes of the three dominant spikes around bounce time show a strong dependence on M_{DM} and can be used as indicators of DM admixing. Assuming that the microphysics inputs can be well constrained in the future, M_{DM} and $\beta_{\text{ic,b}}$ can both be retrieved from the observed GW signals. On the other hand, if the DM core mass $M_{\text{DM}} \geq 0.03 M_{\odot}$, its existence can still be inferred despite the uncertainties of the nuclear matter EOS.

Although our simulations are Newtonian with GR modification of the gravitational potential, we believe that our conclusion on DM effects would not be changed

significantly in full GR modeling since the bounce signal matches quite well to GR simulations with the CFC approximation. The parameterization scheme for electron capture during the collapse phase (Liebendörfer 2005) should not affect our current conclusion qualitatively. However, to investigate the dependence of the PNS g-mode frequency, as well as the explosion energy and ejected mass (and thus light curves) on DM mass, the long-term post-bounce neutrino transport is indispensable. We leave the neutrino-transport simulation and the DM effects on electromagnetic and neutrino signals for a future work.

Acknowledgments — We thank Evan O’Connor for making his neutrino transport code GR1D open-source and stellarcollapse.org for sharing tools of supernova equations of state and several gravitational wave catalogs. We also thank Ken’ichi Nomoto, Bernhard Müller and Ronald Taam for stimulating discussions. This work is partially supported by a grant from the Research Grant Council of Hong Kong (Project 14300317). S.C.L. is supported by World Premier International Research Center Initiative (WPI), MEXT, Japan and JSPS KAKENHI Grant Numbers JP26400222, JP16H02168, JP17K05382. We acknowledge the support of the CUHK Central High Performance Computing Cluster, on which the computation in this work has been performed.

APPENDIX

A. GR1D SIMULATION

A parametrized electron capture scheme is used in the two-dimensional simulations, and the $\rho-Y_e$ profile parametrization is obtained from GR1D (O’Connor 2015) simulations. GR1D solves the neutrino transport problem with a two-moment method with an analytic closure (the so-called M1 scheme), and the most important neutrino emission, absorption, and scattering reactions are included with the rates provided by NuLib (Table 1 in O’Connor 2015). The parameters used for this neutrino transport simulation are similar to those used in a $15 M_{\odot}$ core-collapse simulation presented in the code paper. Fig. A1 shows the results of GR1D simulations with the LS220 EOS, including central density evolution, post-bounce shock propagation, and luminosity and root mean squared (rms) energy of neutrinos. These results are consistent with those in the literature (Dessart et al. 2006; Kitaura et al. 2006).

B. EOS DEPENDENCE

In this appendix, we study the effects of different EOS models on rotating AIC simulations without DM admixture, with the parametrized profiles ($\rho-Y_e$) from GR1D simulations with different EOSs. The initial WD has a $\Omega_{\text{ini}} = 5$ rad/s. The chosen EOSs are the widely used ones, HShen (Shen et al. 2011), LS220 (Lattimer & Swesty 1991), and SFHo (Steiner et al. 2013), which represent high, moderate, and low stiffness. They all satisfy the constraint imposed by the precise measurement of maximum pulsar mass (Pulsar J0348+0432, $2.01 \pm 0.04 M_{\odot}$, Antoniadis et al. (2013)). Note that although SFHo is declared to be the most consistent to all constraints for nuclear matter EOSs, the reason is that the relativistic mean field (RMF) parameters come from optimizing the fitting likelihood to the neutron star mass-radius curve. So for our major goal of investigating DM effects, we choose the most explored LS220 EOS as the standard. The resulting GWs and their spectra are presented in Fig. B1. The waveforms are almost identical around the time of core bounce, except for tiny differences in the GW amplitude ($h_{2,3}$), while the post-bounce ring-down

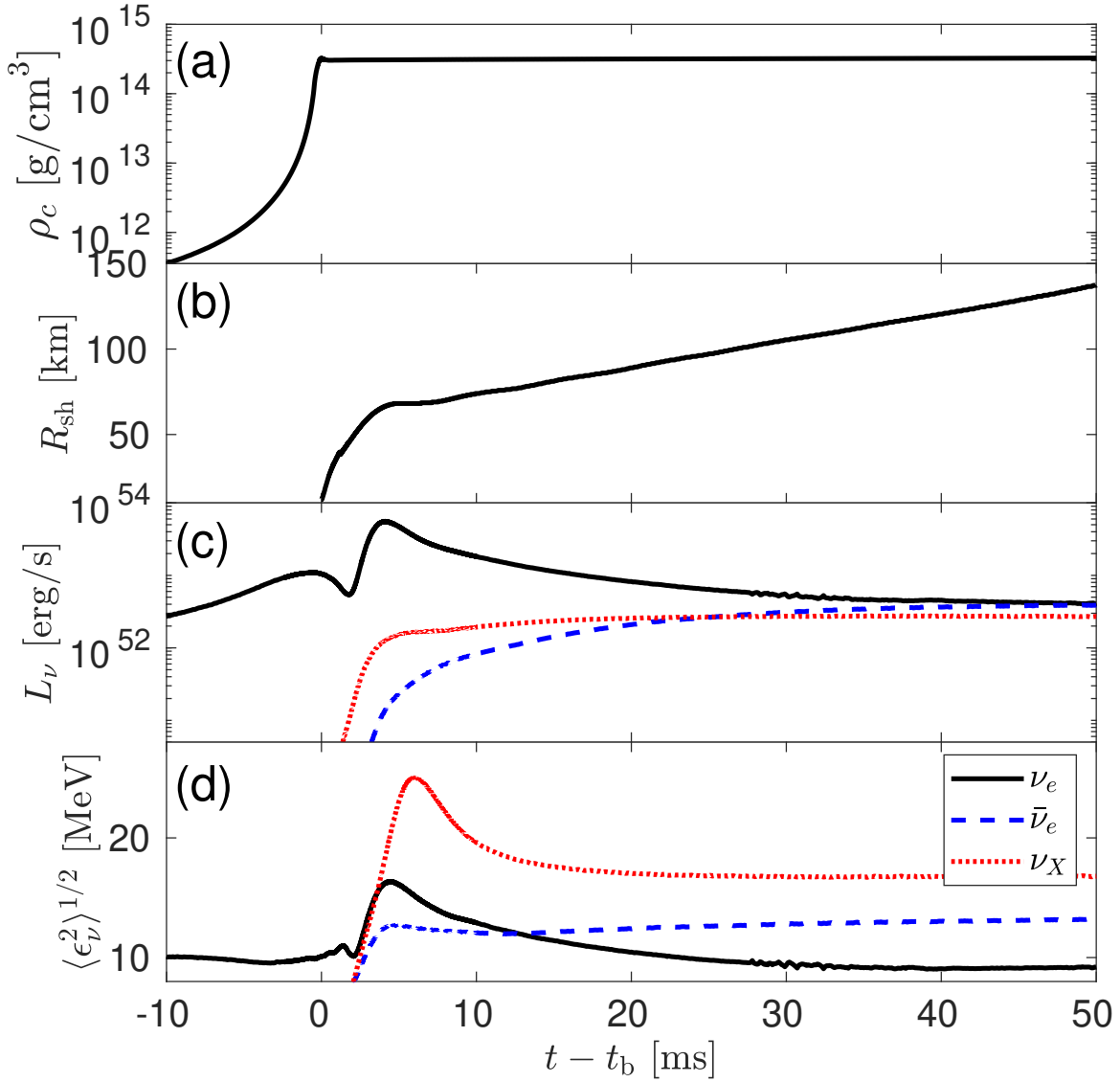


Figure A1. Time evolution of a) central density, b) post-bounce shock propagation, c) neutrino luminosities, and d) rms energy of neutrinos from a spherically symmetric AIC simulation using the GR1D code, with the LS220 EOS.

signals show quasi-periodic cycles with different periods. It is further found that if the GW frequency is normalized with the dynamical frequency

$$f_{\text{dyn}} = \sqrt{G\rho_c}, \quad (\text{B1})$$

the differences in peak frequencies of the prominent GW modes disappear, and the different EOSs give very similar spectra with slightly different amplitudes.

C. CENTRAL DENSITY OF THE PROGENITOR WD

As discussed in Section 2.1, the initial central density ρ_c of an AIC progenitor has not been accurately determined from stellar evolution calculations yet. Three different initial ρ_c ($5.0, 2.5, 1.0 \times 10^{10} \text{ g/cm}^3$) have been used to test the variations in bounce GW signal, with $\Omega_{\text{ini}} = 5, 5, 4 \text{ rad/s}$ and $\beta_{\text{ic,b}} = 1.52, 3.7, 7.2\%$. Hydrodynamical simulations are performed with the same settings such as LS220 EOS and the $Y_e(\rho)$ relation. Their waveforms with rescaled GW amplitudes to match h_1 are shown in Fig. C1. The excellent match of the first three spikes suggests that the variations in the ratios h_2/h_1 and h_3/h_1 for different initial ρ_c are very small. Therefore, the usage of these ratios for identifying DM admixture is not affected by the uncertainty in ρ_c of the AIC progenitor.

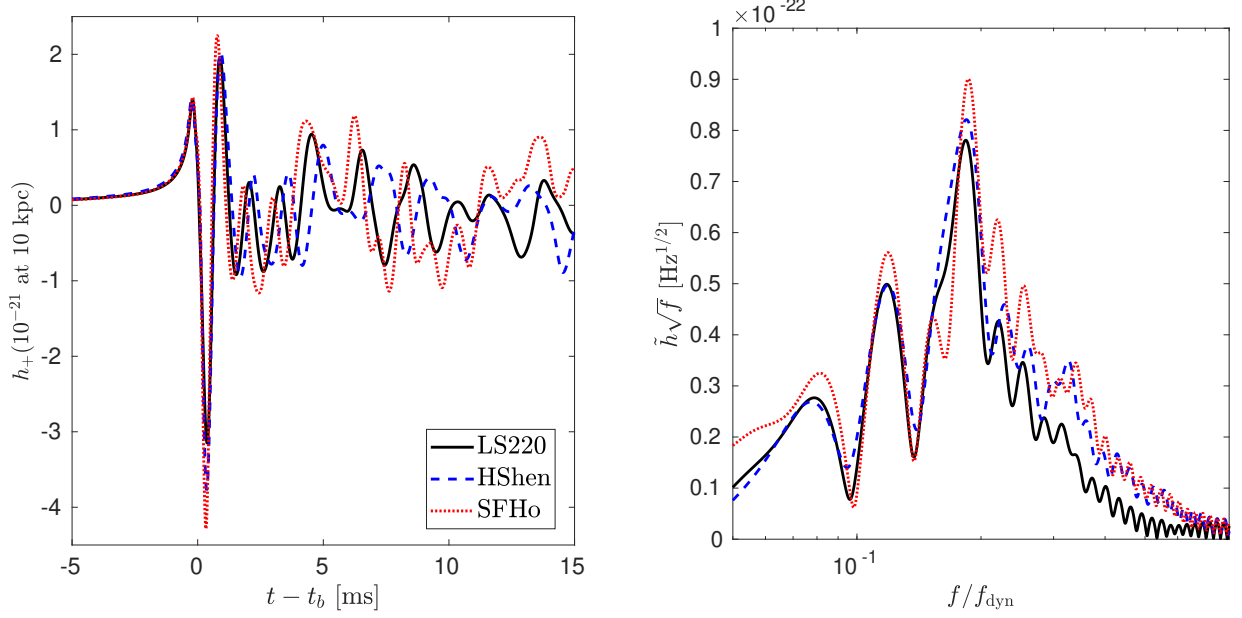


Figure B1. GW waveforms (left) and their Fourier spectra (right) from the AIC of a rotating WD ($\Omega_{\text{ini}} = 5$ rad/s) with three different nuclear matter EOSs. In the spectra, the frequency has been normalized to the dynamical frequency f_{dyn} defined in Eq. B1.

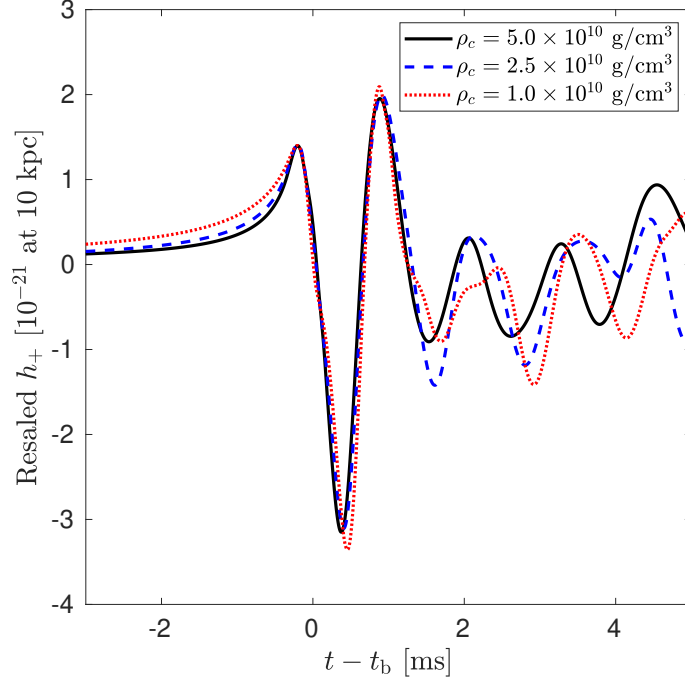


Figure C1. GW waveforms from the AICs of rotating WDs with three different initial ρ_c (Ω_{ini}), 5.0×10^{10} g/cm 3 (5 rad/s), 2.5×10^{10} g/cm 3 (5 rad/s), 1.0×10^{10} g/cm 3 (4 rad/s), all with LS220 EOS. The GW amplitudes are multiplied by a constant to match the peak amplitudes before bounce (h_1).

D. CONVERGENCE TEST

The convergence of GW waveform for the same model, but simulated with different resolutions, has been an issue for the CCSN community (Ott 2009). In a non-rotating model, the asphericity comes from convective motions seeded by stochastic perturbations, eg. grid noise, and so a precise match of GW waveform for different resolutions is not

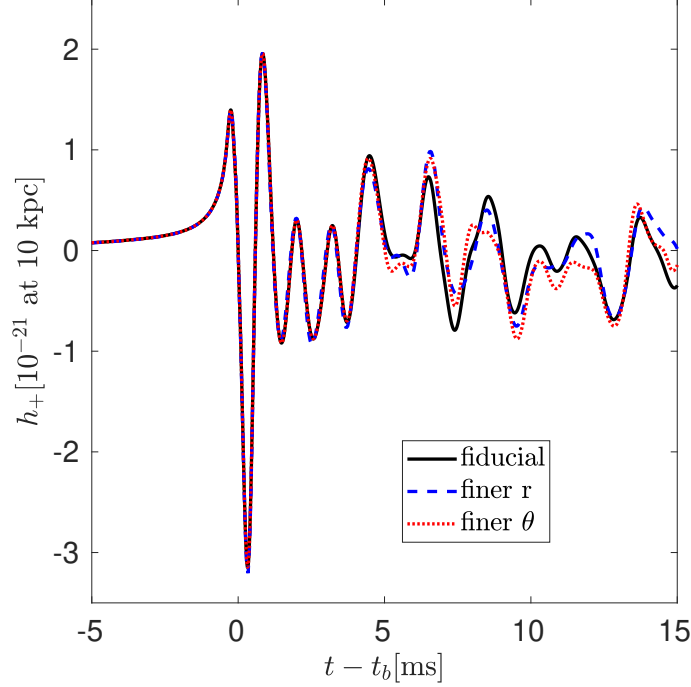


Figure D1. Convergence test for GW waveform of the R5-DM0 model, with different resolutions. The fiducial run is with 2° for θ grid and 370 m for r grid near the center. Finer r is with the same θ grid as the fiducial run and 220 m for the r grid near the center. Finer θ is with 1.5° for the θ grid and the same r grid as the fiducial run.

expected. Nonetheless, in our non-rotating and DM-absent AIC model, the GW emission from convection emerges after 10 ms postbounce and the maximum h_+ reaches $\sim 0.1 \times 10^{-21}$ at 10 kpc. This is a factor of 5 smaller than the slowest rotating model in this paper. To check the convergence for the rotating models, we performed two additional simulations with higher resolutions for the moderately rotating AIC model (R5-DM0, $\rho_{c,\text{ini}} = 5 \times 10^{10} \text{ g/cm}^3$ and $\Omega_{\text{ini}} = 5 \text{ rad/s}$). The resulting GW waveforms are compared with that of the fiducial run in Fig. D1. Remarkably, the waveforms match excellently for $t \lesssim t_b + 5 \text{ ms}$, while the later oscillations differ slightly due to the contribution from convection.

E. EXTENDED TABLE FOR THE RESULTS OF ALL THE MODELS

Table E1. Extended table for the results of the models with a specified initial angular velocity Ω_{ini} and admixed DM mass M_{DM} . M_{NM} is the NM mass. J is the total initial angular momentum. β_{ini} and $\beta_{\text{ic,b}}$ are the initial ratio of rotational energy to gravitational energy and that of the inner core at the bounce. R_{e} and R_{p} are the equatorial and polar radii of the white dwarfs, respectively. t_{b} , $\rho_{\text{c,b}}$ and $M_{\text{ic,b}}$ are the time, central density and mass of the inner core at the bounce. M_{PNS} is the PNS mass at 50 ms after the bounce.

Model	Ω_{ini} [rad/s]	M_{DM} [M_{\odot}]	M_{NM} [M_{\odot}]	J [$10^{50} \text{ erg} \cdot \text{s}$]	β_{ini} [%]	R_{e} [km]	$R_{\text{p}}/R_{\text{e}}$	$\beta_{\text{ic,b}}$ [%]	t_{b} [ms]	$\rho_{\text{c,b}}$ [10^{14} g/cm^3]	$M_{\text{ic,b}}$ [M_{\odot}]	M_{PNS} [M_{\odot}]
R0-DM0	0.0	0	1.448	–	–	816	1	–	32.8	3.99	0.56	1.26
R0-DM1	0.0	0.01	1.402	–	–	888	1	–	37.7	3.90	0.54	1.21
R0-DM2	0.0	0.02	1.355	–	–	977	1	–	45.2	3.80	0.53	1.15
R0-DM3	0.0	0.03	1.304	–	–	1113	1	–	58.6	3.69	0.51	1.07
R0-DM4	0.0	0.04	1.249	–	–	1313	1	–	86.1	3.55	0.49	0.99
R2-DM0	2.0	0	1.450	0.04	0.04	820	0.995	0.25	32.9	3.98	0.56	1.26
R2-DM1	2.0	0.01	1.405	0.04	0.05	893	0.990	0.34	37.8	3.88	0.55	1.20
R2-DM2	2.0	0.02	1.358	0.05	0.07	987	0.990	0.50	45.4	3.77	0.54	1.13
R2-DM3	2.0	0.03	1.309	0.06	0.11	1130	0.980	0.86	59.0	3.63	0.53	1.05
R2-DM4	2.0	0.04	1.257	0.08	0.19	1347	0.970	1.71	87.3	3.44	0.51	0.96
R3-DM0	3.0	0	1.451	0.05	0.09	828	0.985	0.55	33.0	3.94	0.56	1.26
R3-DM1	3.0	0.01	1.407	0.06	0.12	902	0.980	0.75	38.0	3.83	0.55	1.20
R3-DM2	3.0	0.02	1.361	0.07	0.16	1002	0.970	1.13	45.6	3.71	0.55	1.12
R3-DM3	3.0	0.03	1.314	0.09	0.25	1159	0.956	1.91	59.3	3.52	0.54	1.03
R3-DM4	3.0	0.04	1.266	0.13	0.43	1395	0.932	3.77	88.4	3.26	0.53	0.93
R3.5-DM0	3.5	0	1.453	0.06	0.12	832	0.980	0.75	33.0	3.92	0.57	1.25
R3.5-DM1	3.5	0.01	1.409	0.07	0.16	902	0.975	1.03	38.1	3.81	0.56	1.19
R3.5-DM2	3.5	0.02	1.364	0.09	0.22	1007	0.966	1.53	45.8	3.67	0.56	1.11
R3.5-DM3	3.5	0.03	1.318	0.11	0.34	1165	0.946	2.59	59.7	3.47	0.55	1.02
R3.5-DM4	3.5	0.04	1.273	0.16	0.60	1430	0.900	4.88	89.4	3.13	0.55	0.91
R5-DM0	5.0	0	1.458	0.09	0.25	849	0.956	1.52	33.2	3.85	0.59	1.25
R5-DM1	5.0	0.01	1.416	0.11	0.33	934	0.942	2.11	38.4	3.73	0.59	1.17
R5-DM2	5.0	0.02	1.374	0.13	0.46	1043	0.928	3.12	46.3	3.55	0.58	1.09
R5-DM3	5.0	0.03	1.333	0.16	0.71	1243	0.896	5.09	60.9	3.23	0.59	0.99
R5-DM4 ^a	5.0	0.04	1.303	0.25	1.33	1809	0.726	8.81	93.1	2.73	0.59	0.87
R7-DM0	7.0	0	1.469	0.13	0.50	875	0.918	2.98	33.6	3.74	0.63	1.23
R7-DM1	7.0	0.01	1.430	0.15	0.66	982	0.900	4.10	39.0	3.55	0.63	1.15
R7-DM2	7.0	0.02	1.394	0.19	0.94	1147	0.852	5.86	47.3	3.27	0.63	1.05
R9-DM0	9.0	0	1.485	0.18	0.86	939	0.869	4.89	34.2	3.57	0.66	1.19
R9-DM1	9.0	0.01	1.451	0.21	1.15	1113	0.794	6.50	39.8	3.31	0.67	1.11
Rmax-DM0	10.9	0	1.506	0.23	1.32	1165	0.673	6.92	34.9	3.37	0.70	1.17
Rmax-DM1	9.5	0.01	1.459	0.23	1.30	1256	0.680	7.10	40.1	3.24	0.68	1.10
Rmax-DM2	8.0	0.02	1.409	0.23	1.27	1333	0.708	7.27	48.0	3.10	0.66	1.03
Rmax-DM3	6.50	0.03	1.358	0.23	1.28	1519	0.704	7.76	62.5	2.90	0.63	0.96

^aAlso Rmax-DM4.

Table E2. Same as Table E1 but for the models with a specified $\beta_{ic,b}$ and admixed DM mass M_{DM} . Some models are the same as those in Table E1.

Model	Ω_{ini} [rad/s]	M_{DM} [M_{\odot}]	M_{NM} [M_{\odot}]	J [$10^{50} \text{ erg} \cdot \text{s}$]	β_{ini} [%]	R_e [km]	R_p/R_e	$\beta_{ic,b}$ [%]	t_b [ms]	$\rho_{c,b}$ [10^{14} g/cm^3]	$M_{ic,b}$ [M_{\odot}]	M_{PNS} [M_{\odot}]
$\beta 1\text{-DM0}$	4.1	0	1.455	0.07	0.17	832	0.975	1.00	33.1	3.90	0.58	1.25
$\beta 1\text{-DM1}^a$	3.5	0.01	1.409	0.07	0.16	902	0.975	1.03	38.1	3.81	0.56	1.19
$\beta 1\text{-DM2}^b$	3.0	0.02	1.361	0.07	0.16	1002	0.970	1.13	45.6	3.71	0.55	1.12
$\beta 1\text{-DM3}$	2.2	0.03	1.309	0.07	0.12	1130	0.980	0.99	59.1	3.61	0.53	1.04
$\beta 1\text{-DM4}$	1.5	0.04	1.253	0.06	0.10	1333	0.985	0.91	86.8	3.50	0.50	0.96
$\beta 3\text{-DM0}^c$	7.0	0	1.469	0.13	0.50	875	0.918	2.98	33.6	3.74	0.63	1.23
$\beta 3\text{-DM1}$	6.1	0.01	1.423	0.13	0.49	948	0.918	3.08	38.7	3.64	0.61	1.16
$\beta 3\text{-DM2}^d$	5.0	0.02	1.374	0.13	0.46	1043	0.928	3.12	46.3	3.51	0.58	1.09
$\beta 3\text{-DM3}$	3.8	0.03	1.321	0.12	0.41	1176	0.932	3.12	60.0	3.43	0.56	1.01
$\beta 3\text{-DM4}$	1.3	0.04	1.263	0.12	0.35	1374	0.946	3.10	88.1	3.33	0.53	0.94
$\beta 6\text{-DM0}$	10.0	0	1.495	0.21	1.09	997	0.790	6.00	34.6	3.46	0.68	1.18
$\beta 6\text{-DM1}$	8.6	0.01	1.447	0.20	1.04	1070	0.802	6.03	39.7	3.36	0.66	1.13
$\beta 6\text{-DM2}$	7.1	0.02	1.396	0.19	0.97	1159	0.818	6.03	47.5	3.26	0.63	1.05
$\beta 6\text{-DM3}$	5.6	0.03	1.341	0.19	0.90	1294	0.839	6.06	61.5	3.11	0.60	0.98
$\beta 6\text{-DM4}$	4.0	0.04	1.281	0.18	0.79	1481	0.865	5.94	90.4	2.99	0.56	0.90

^aAlso the model R3.5-DM1.^bAlso the model R3-DM2.^cAlso the model R7-DM0.^dAlso the model R5-DM2.

REFERENCES

- Abdikamalov, E. B., Ott, C. D., Rezzolla, L., et al. 2010, *PhRvD*, 81, 044012
- Andresen, H., Müller, E., Janka, H. T., et al. 2019, *MNRAS*, 486, 2238
- Antoniadis, J., Freire, P. C. C., Wex, N., et al. 2013, *Science*, 340, 448
- Baiotti, L., de Pietri, R., Manca, G. M., & Rezzolla, L. 2007, *PhRvD*, 75, 044023
- Barkana, R. 2018, *Nature*, 555, 71
- Barsotti, L., Fritschel, P., Evans, M., & Gras, S. 2018, *Tech. Rep. LIGO-T1800042-v5*.
dcc.ligo.org/LIGO-T1800042/public
- Bertone, G., & Hooper, D. 2018, *RvMP*, 90, 045002
- Bowman, J. D., Rogers, A. E. E., Monsalve, R. A., Mozdzen, T. J., & Mahesh, N. 2018, *Nature*, 555, 67
- Bramante, J. 2015, *PhRvL*, 115, 141301
- Brito, R., Cardoso, V., & Okawa, H. 2015, *PhRvL*, 115, 111301
- Cerdá-Durán, P., DeBrye, N., Aloy, M. A., Font, J. A., & Obergaulinger, M. 2013, *ApJ*, 779, L18
- Cerdá-Durán, P., Quilis, V., & Font, J. A. 2007, *CoPhC*, 177, 288
- Cermeño, M., Pérez-García, M. Á., & Silk, J. 2017, *PASA*, 34, e043
- Choplin, A., Coc, A., Meynet, G., et al. 2017, *A&A*, 605, A106
- Dessart, L., Burrows, A., Ott, C. D., et al. 2006, *ApJ*, 644, 1063
- Dimmelmeier, H., Font, J. A., & Müller, E. 2002, *A&A*, 393, 523
- Dimmelmeier, H., Ott, C. D., Marek, A., & Janka, H.-T. 2008, *PhRvD*, 78, 064056
- Einasto, J., Saar, E., Kaasik, A., & Chernin, A. D. 1974, *Nature*, 252, 111
- Ellis, J., Hütsi, G., Kannike, K., et al. 2018, *PhRvD*, 97, 123007
- Farrow, N., Zhu, X.-J., & Thrane, E. 2019, *ApJ*, 876, 18
- Fink, M., Kromer, M., Hillebrandt, W., et al. 2018, *A&A*, 618, A124
- Finn, L. S., & Evans, C. R. 1990, *ApJ*, 351, 588
- Fryer, C., Benz, W., Herant, M., & Colgate, S. A. 1999, *ApJ*, 516, 892
- Fuller, J., & Ott, C. D. 2015, *MNRAS*, 450, L71
- Gossan, S. E., Sutton, P., Stuver, A., et al. 2016, *PhRvD*, 93, 042002
- Graham, P. W., Janish, R., Narayan, V., Rajendran, S., & Riggins, P. 2018, *PhRvD*, 98, 115027

- Graham, P. W., Rajendran, S., & Varela, J. 2015, *PhRvD*, 92, 063007
- Hachisu, I. 1986, *ApJS*, 61, 479
- Hansen, C. J., Primas, F., Hartman, H., et al. 2012, *A&A*, 545, A31
- Hild, S., Abernathy, M., Acernese, F., et al. 2011, *CQGra*, 28, 094013
- Hillebrandt, W., Kromer, M., Röpke, F. K., & Ruiter, A. J. 2013, *FrPhy*, 8, 116
- Janka, H.-T. 2012, *ARNPS*, 62, 407
- Jones, S., Röpke, F. K., Fryer, C., et al. 2019, *A&A*, 622, A74
- Kitaura, F. S., Janka, H.-T., & Hillebrandt, W. 2006, *A&A*, 450, 345
- Kouvaris, C., & Nielsen, N. G. 2015, *PhRvD*, 92, 063526
- Lattimer, J. M., & Swesty, F. D. 1991, *NuPhA*, 535, 331
- Lee, J., & Komatsu, E. 2010, *ApJ*, 718, 60
- Leung, S.-C., Chu, M.-C., & Lin, L.-M. 2011, *PhRvD*, 84, 107301
- . 2015a, *ApJ*, 812, 110
- . 2015b, *MNRAS*, 454, 1238
- Leung, S.-C., Chu, M.-C., Lin, L.-M., & Wong, K.-W. 2013, *PhRvD*, 87, 123506
- Leung, S.-C., & Nomoto, K. 2018, *ApJ*, 861, 143
- . 2019, arXiv e-prints, arXiv:1901.10007
- Leung, S.-C., Nomoto, K., & Suzuki, T. 2019, arXiv e-prints, arXiv:1901.11438
- Leung, S. C., Zha, S., Chu, M. C., Lin, L. M., & Nomoto, K. 2019, in prep.
- Liebendörfer, M. 2005, *ApJ*, 633, 1042
- Liu, X.-D., Osher, S., & Chan, T. 1994, *JCoPh*, 115, 200
- Marek, A., Dimmelmeier, H., Janka, H.-T., Müller, E., & Buras, R. 2006, *A&A*, 445, 273
- Martinez, J. G., Stovall, K., Freire, P. C. C., et al. 2015, *ApJ*, 812, 143
- Moenchmeyer, R., Schaefer, G., Mueller, E., & Kates, R. E. 1991, *A&A*, 246, 417
- Morozova, V., Radice, D., Burrows, A., & Vartanyan, D. 2018, *ApJ*, 861, 10
- Mukhopadhyay, P., & Schaffner-Bielich, J. 2016, *PhRvD*, 93, 083009
- Müller, B., Janka, H.-T., & Marek, A. 2013, *ApJ*, 766, 43
- Murphy, J. W., Ott, C. D., & Burrows, A. 2009, *ApJ*, 707, 1173
- Nagakura, H., Furusawa, S., Togashi, H., et al. 2019, *ApJS*, 240, 38
- Nomoto, K., & Kondo, Y. 1991, *ApJL*, 367, L19
- O'Connor, E. 2015, *ApJS*, 219, 24
- Oertel, M., Hempel, M., Klähn, T., & Typel, S. 2017, *RvMP*, 89, 015007
- Ott, C. D. 2009, *CQGra*, 26, 063001
- Ott, C. D., Abdikamalov, E., O'Connor, E., et al. 2012, *PhRvD*, 86, 024026
- Özel, F., Psaltis, D., Narayan, R., & Santos Villarreal, A. 2012, *ApJ*, 757, 55
- Pajkos, M. A., Couch, S. M., Pan, K.-C., & O'Connor, E. P. 2019, arXiv e-prints, arXiv:1901.09055
- Pan, K.-C., Liebendörfer, M., Couch, S. M., & Thielemann, F.-K. 2018, *ApJ*, 857, 13
- Piro, A. L., & Kulkarni, S. R. 2013, *ApJL*, 762, L17
- Piro, A. L., & Thompson, T. A. 2014, *ApJ*, 794, 28
- Planck Collaboration, Aghanim, N., Akrami, Y., et al. 2018, arXiv e-prints, arXiv:1807.06209
- Radice, D., Morozova, V., Burrows, A., Vartanyan, D., & Nagakura, H. 2019, *ApJ*, 876, L9
- Reisswig, C., & Pollney, D. 2011, *Classical and Quantum Gravity*, 28, 195015
- Ren, X., Zhao, L., Abdukerim, A., et al. 2018, *PhRvL*, 121, 021304
- Richers, S., Ott, C. D., Abdikamalov, E., O'Connor, E., & Sullivan, C. 2017, *PhRvD*, 95, 063019
- Ruiter, A. J., Ferrario, L., Belczynski, K., et al. 2019, *MNRAS*, 484, 698
- Schwab, J., Bildsten, L., & Quataert, E. 2017, *MNRAS*, 472, 3390
- Schwab, J., Podsiadlowski, P., & Rappaport, S. 2010, *ApJ*, 719, 722
- Schwab, J., & Rocha, K. A. 2019, *ApJ*, 872, 131
- Shen, H., Toki, H., Oyamatsu, K., & Sumiyoshi, K. 2011, *ApJS*, 197, 20
- Skinner, M. A., Burrows, A., & Dolence, J. C. 2016, *ApJ*, 831, 81
- Steiner, A. W., Hempel, M., & Fischer, T. 2013, *ApJ*, 774, 17
- Torres-Forné, A., Cerdá-Durán, P., Obergaulinger, M., Müller, B., & Font, J. A. 2019, arXiv e-prints, arXiv:1902.10048
- Vartanyan, D., Burrows, A., Radice, D., Skinner, M. A., & Dolence, J. 2019, *MNRAS*, 482, 351
- Wang, B. 2018, *MNRAS*, 481, 439
- Xiang, Q.-F., Jiang, W.-Z., Zhang, D.-R., & Yang, R.-Y. 2014, *PhRvC*, 89, 025803
- Yoon, S.-C., & Langer, N. 2004, *A&A*, 419, 623